Measurement Science and Technology

Check for updates

OPEN ACCESS

RECEIVED
6 March 2026

REVISED
16 June 2026

ACCEPTED FOR PUBLICATION
10 July 2026

PUBLISHED
24 July 2026

Original content from this work may be used under the terms of the Creative Commons Attribution 4.0 licence.

Any further distribution of this work must maintain attribution to the author(s) and the title of the work, journal citation and DOI.

PAPER

Automatic, single-sweep, cuvette-based determination of A_2 (B_{22}), K_D, and other equilibrium properties for macromolecules

Curtis W Jarand and Wayne F Reed*

Tulane University, New Orleans, LA 70118, United States of America

* Author to whom any correspondence should be addressed.

E-mail: wreed@tulane.edu

Keywords: automatic polymer characterization, light scattering, A_2 and k_D, protein and polysaccharide characterization, automatic continuous dilution

Abstract

The second virial coefficient A_2 (B_{22}) and diffusion interaction parameter k_D are used to assess colloidal stability and the risk of undesirable high viscosity behavior of monoclonal antibodies and other biologics at high concentration. These processes have conventionally been conducted through discrete serial dilutions or multiple measurements at various concentrations in a well-plate. Here, a single trajectory experiment is performed via an automatic cuvette-based method to produce continuous dilution of the starting concentration of the material, that is, automatic continuous dilution (ACD), while gathering static light scattering and/or dynamic light scattering data during the process. The sample volume in the cuvette is kept constant during the process, and the measurements are made without disturbance or motion of the spatial orientation of the incident laser beam and cuvette. This single-sweep approach yields weight average molar mass M_w, A_2 (B_{22}), apparent hydrodynamic diameter $D_{H,app}$, k_D, and, where measurable, A_3. The method reduces sample consumption and eliminates artifacts due to plate motion, thereby increasing reliability and reproducibility. The sample can be recovered after the measurements, as the final withdrawal reservoir volume is only about 5× the cuvette volume. Examples include two globular proteins, where A_2 is positive and k_D small, which are expected for globular proteins resembling spheres. For natural polyelectrolytes, A_2 and an "effective k_D" are both strongly positive for sodium hyaluronate and A_2 is strongly positive. In contrast, effective k_D is strongly negative for alginate. This reflects the effects of segment overlap and interactions for random coil polymers, which makes the effective k_D dramatically different than for k_D of spheres. This concise method may prove useful and economical for assessing formulation stability and providing an indication of high viscosity behavior. ACD can also be used directly with any instrument accepting 1 cm cuvettes to determine the impact of dilution on association states and other concentration-dependent phenomena.

1. Introduction

Stabilizing biologic formulations and assessing their high concentration viscosity behavior are critical development objectives in the biotechnology sector. Biologics are increasingly successful in therapeutic applications and include monoclonal antibodies (mAbs) and other proteins, peptides, mRNA, lipid nanoparticles, agents for gene therapy, polysaccharides, protein–polysaccharide conjugate vaccines, and others. Two major characterization parameters are the second virial coefficient, A_2 (B_{22}) and the diffusion interaction parameter, k_D [1–3]. In short, A_2 thermodynamically averages the energetic interactions between two particles over all mutual orientations and distances, and is directly related to their mutual hard and soft (e.g. electrostatic) excluded volume. k_D, the diffusion interaction parameter, is inherently more complicated since it involves both spatial excluded volume and long-range hydrodynamic interactions between particles.

© 2026 The Author(s). Published by IOP Publishing Ltd

A_2 is a good indicator of the colloidal stability of a macromolecular or colloidal solution. This makes it an essential characteristic for stabilizing biologic formulations. In general, the higher the value of A_2, the more stable the biologic formulation. Low and negative values of A_2 generally signal a greater propensity for aggregation.

In contrast, k_D is related both to thermodynamic stability (A_2) and purely hydrodynamic interactions between particles, via the hydrodynamic term k_H. Since there is intense interest in the biotechnology sector to produce high-concentration mAb formulations, the viscosity behavior of mAbs at high concentration becomes crucial. The motive for producing high concentration formulations is to allow parenteral injection at high concentrations, rather than slow IV drips, typically lasting an hour or more, at low concentrations.

k_D does not reliably predict the high viscosity behavior of mAb and other biologic formulations since its hydrodynamic component is not actually related to viscosity, but rather deals only with long-range two-body hydrodynamic interactions. In addition, three-body and higher interactions quickly become essential as biologic concentration increases, and these effects transcend the simple two-body interactions and include overlap interactions, shape parameters, cluster kinetics, and other complex factors not predictable merely from k_D. Given that k_D is inadequate for forecasting high concentration biologic diffusive behavior—and is not directly predictive of low or high concentration viscosity—it has nonetheless become a critical screening tool since it is easy to measure with dynamic light scattering (DLS) and requires only low amounts of scarce biologic material. High values of k_D imply a better chance of low viscosity at high concentrations, whereas low positive, or negative, values can imply the risk of higher viscosities at high concentrations.

From a measurement science perspective, the determination of A_2 and k_D traditionally relies on a series of discrete measurements on independently prepared concentrations. For single sample nonflow instruments, this may increase errors due to sample preparation and scattering impurities, leading to a lower density of points, far longer measurement cycles, and results with higher uncertainty. The presence of scattering impurities, such as "dust," can render measurements of later serial dilutions unusable. For flow-based systems, the samples are also usually discrete and may involve more expensive sample preparation and light scattering instrumentation. For systems that use robotics to prepare many samples in microwells that move with respect to a single incident beam and detection optics, additional sources of scattering artifacts may arise due to well edge effects, stray light, meniscus and evaporation effects. Although robotic systems can be largely automated, they are complex and expensive, compared to the automatic dilution of a single initial sample in a standard 1 cm cuvette, which produces a continuum of concentrations.

Automated characterizations using continuous dilution have been explored, including earlier work using a light-scattering flow cell, capillary viscometer, a differential refractometer, and continuous dilution trajectory [4]. Since these systems require relatively large sample volumes, they are well suited to the studies of inexpensive synthetic polymers but less applicable to biologic formulations where the material is often scarce [5, 6]. Other researchers subsequently used both continuous dilution in a flow cell and discrete dilution in a cuvette with static light scattering (SLS) to investigate the binding properties and nonideality of proteins [7, 8]. Correspondigly, discrete stop-flow, automated composition-gradient light-scattering methods, including Wyatt CG–MALS implementations using flow cells, have been used for biomolecular interaction analysis and nonideal solution behavior [9, 10]. The primary novelty of the current device and method, compared to the previous continuous dilution trajectory [4], is that a simple, disposable 1 cm cuvette can be used (nondisposable cuvettes can also be used), with much less sample, which is also recoverable, and DLS has been added. Furthermore, since the shape of the concentration trajectory is known analytically from equation (11), the refractometer, used for concentration determination with binary mixing pumps, is no longer needed.

The present work adapts this trajectory-based measurement concept to a single-cuvette automatic continuous dilution (ACD) format compatible with the small sample volumes typical of biologics research. The method reduces the trajectory-based measurement idea to a standard cuvette format with minimal fluidic complexity.

By maintaining a fixed optical geometry while continuously diluting the sample within the cuvette, the method produces a time-resolved dataset from which the concentration dependence of scattering intensity and diffusion coefficient can be extracted. This allows the determination of parameters, such as M_w, A_2, and k_D, via a single concentration trajectory, reducing experimental handling steps and providing continuous data points.

The method can be used with any existing light-scattering instrument, or any other spectroscopic instrument, that accepts 1 cm cuvettes, without modification. The technique is hence a general measurement approach for determining concentration-dependent macromolecular properties with reduced number of samples and improved experimental consistency.

1.1. Relationship among A_2, k_D, and viscosity, η

The conceptual relationship among A_2, k_D, and η is worth a closer look. As mentioned, A_2 integrates pair-wise energetic interactions over all mutual orientations between the particles of mutual separation r. If the particles are charged, as are all those dealt with in this work, then the electrostatic interactions are screened by the added electrolyte and die off as $e^{-\kappa r}/r$, where η is the Debye screening parameter and r is the distance between particles. A_2 directly affects the colloidal stability of the solution, such as its propensity to develop associations and aggregates. In contrast, when the first-order hydrodynamic perturbation dies off as $1/r$, there is no equivalent screening term, and they exist apart from interparticle potentials, because it is the viscous motion of the intervening fluid between the particles that controls them, not the interparticle potential. This can also lead to collective hydrodynamic effects. In general, the hydrodynamic interactions have a longer range than the interparticle potentials and can often dominate k_D.

It is easy to imagine how a particle in directed or diffusive motion entrains the fluid around it, and perturbs the fluid flow field at distances far from the particle itself. A second particle can feel this perturbation and have its own motion in the same direction enhanced, that is, its hydrodynamic drag decreased. In contrast, depending on the type of motion, for example, vortical plus translational, the perturbation can work to impede, or increase the second particle's hydrodynamic drag. Hydrodynamic theories often start with the Stokes form of the Navier–Stokes equation for viscous, incompressible fluids, in the limit of low Reynolds number and for steady-state flow. The fundamental solution to this involves the Oseen tensor, which represents viscous perturbations up to first order and is long range [11–13]. These theories have been highly developed and are beyond the scope of this work to elaborate further on.

k_D refers here to values obtained from the diffusion coefficients obtained by DLS. To first order, k_D relates the mutual diffusion coefficient measured at finite concentration, $D_m(c)$ to the self-diffusion coefficient D_0 obtained by extrapolating $D_m(c)$ to $c = 0$;

$$D_m(c) = D_0\left(1 + k_D c + O\left(c^2\right)\right) \tag{1}$$

where $O\left(c^2\right)$ represents terms in c^2 and higher order. The plot of $D_m(c)$ vs c at low c (i.e. where $O\left(c^2\right)$ terms are negligible) yields both D_0 and k_D. The fact that k_D contains both thermodynamic and hydrodynamic information is often expressed, for dilute, nonoverlapping hard spheres, as follows:

$$k_D = 2A_2^* + k_H \tag{2}$$

where k_H is the purely hydrodynamic part, and $A_2^* = A_2 M_w$, which then gives consistent units of $cm^3\ g^{-1}$ for all terms in equation (2). For dilute hard spheres k_D and k_H are often positive, but this is no longer generally true for random coils and other polymer morphologies, especially in the semidilute regime, for which it is possible that k_H and hence also k_D can be negative.

It is possible, however, that even if $A_2 > 0$, $k_H < 0$, so that k_D may be negative. This can occur, for example, in cases where there is high hydrodynamic drag and relatively weak thermodynamic repulsion. In contrast, if $A_2 < 0$ and if there is a strong positive hydrodynamic interaction, then k_D can be positive. Note that equation (2) breaks down completely while dealing with polymers in the semidilute regime, and for polyelectrolytes resembling charged random coils in the early overlap concentration regime, where chain–chain overlap, entanglement, and possible microgel clustering can occur.

Importantly, even though the primary motive for determining k_D is to assess the high viscosity behavior of solutions, it is emphasized that k_D, which is related to diffusive behavior, is not directly or simply quantitatively related to solution viscosity, η, even at low concentration, which is often expressed as follows:

$$\eta = \eta_0\left(1 + [\eta]c + K_H^{\text{Huggins}}[\eta]^2 c^2 + O\left(c^3\right)\right) \tag{3}$$

where η_0 is the viscosity of the solvent, and $[\eta]$ is the solute intrinsic viscosity related to its hydrodynamic volume V_H and molar mass M by the proportionality:

$$[\eta] \propto \frac{V_H}{M}. \tag{4}$$

In equation (3), $K_H^{Huggins}$ is the dimensionless Huggins viscosity parameter, related to viscous flow under applied stress, typically between 0.2 and 0.8, and should never be confused with the hydrodynamic term k_H in equation (2). The diffusion-based k_H (units of $cm^3\ g^{-1}$) expresses long-range hydrodynamic interactions, whereas $K_H^{Huggins}$ (dimensionless) relates to near-field interactions, including lubrication effects. These latter refer to the variations in viscosity due to particles approaching each other, requiring the fluid velocity between them to increase appreciably with increasing viscous stress.

This now brings us to the question: what is the actual relevance of k_D for assessing the high viscosity behavior of concentrated biologic formulations? In principle, there is no direct relevance, and there is no general quantitative relation between k_D and viscosity, even at low concentration, since k_D and $K_H^{Huggins}$ have no general quantitative relationship. However, both diffusion and viscosity are hydrodynamic effects, albeit under different paradigms—random Brownian motion, versus stress-induced motion—so that the behavior of diffusion in dilute conditions can act as a crude screen for viscosity even at higher concentrations; for example, a high k_D is more likely to yield a lower viscosity at higher concentrations than a low or negative k_D.

The D_0 normalized derivative of equation (1) with respect to concentration yields k_D; that is, it shows how quickly diffusion is impeded or enhanced as concentration increases,

$$\frac{1}{D_0}\frac{\partial D_m(c)}{\partial c} = k_D. \tag{5}$$

A highly positive k_D implies significant thermodynamic and hydrodynamic repulsion among molecules; hence, the viscosity risk at high concentration should be lower than it would be for low values of k_D; that is, high k_D is desirable for successfully creating high viscosity formulations. High k_D is usually linked to high colloidal stability, often due to strong net molecular charge and repulsive intermolecular interactions. In this sense, A_2 can also assess high viscosity behavior, but since it does not include hydrodynamic effects, it is a weaker indicator of high viscosity behavior than k_D.

In contrast, $k_D < 0$ implies net attractive interactions, which lead to the $O(c^2)$ increasing rapidly, with a corresponding large, undesirable increase in viscosity at higher concentrations.

The theoretical and experimental foundations for k_D and its relation to the high viscosity behavior has been amply documented [14–18], including k_D determination using well-plates [19–23]. It should be pointed out that, in some sense, k_D is a "specialty parameter," mostly used in the development of mAbs but not widely used in general polymer characterization. With this caveat, two nonprotein systems, the polyanions hyaluronate and alginate are measured here, for which A_2 is determined and an "equivalent k_D," which lies beyond the assumptions of k_D for nonoverlapping molecules.

Other methods have also been used to characterize biologic behavior under dilution, especially UV absorption to characterize self-associations at high concentration and upon dilution [24–28].

2. Materials

Bovine serum albumin (BSA) was obtained from Sigma–Aldrich as a lyophilized powder with a purity level of ⩾99%. Low-viscosity alginate was obtained from Alfa Aesar. Lysozyme was obtained from Sigma–Aldrich as a lyophilized powder with a purity of ⩾98%. Sodium hyaluronate was obtained from Thermo Scientific with a purity of 95%. Since biomacromolecules often have some variability in their properties, 51 nm ± 3 nm NIST traceable polystyrene nanosphere latex size standards from Thermo Scientific (Fremont, California), with a nominal stock concentration of 0.01 g cm^{-3}, were used to compare error bars due to instrumentation, from those due to inherent variability in the biomacromolecules. It is noted, however, that these standards have a broad size distribution of ±8.4 nm around the mean, which is highly (poly)disperse.

All the measurements were performed at 25 ± 0.5°C, for which the water viscosity is 0.0089P ± 0.9%.

3. Methods

3.1. SLS determination of A_2

There are several analytical approaches to obtaining A_2 and k_D that aid in these tasks, besides static and dynamic light scattering (SLS and DLS, respectively). For A_2, osmotic pressure measurements [29], sedimentation equilibrium from ultracentrifugation [30], small-angle x-ray scattering [31], and small-angle

neutron scattering [32] can also be used. For k_D, Taylor dispersion analysis [33, 34] and pulse-field gradient NMR diffusion measurements [35, 36] have been employed.

A_2 is typically determined by light scattering, whereas B_{22}, with the same thermodynamic meaning as A_2 ($cm^3-mol\ g^{-2}$), but with different units (volume mol^{-1}), is usually determined by measuring osmotic pressure vs c. They are related in a monodisperse system by $A_2 = \frac{B_{22}}{M^2}$. Although the thermodynamic meanings of A_2 and B_{22} are the same, but with different concentration units, it is essential to note that in a disperse molecular population, the averages represented by A_2 and B_{22} are different, since A_2 is intensity weighted (M^2) over the population, whereas B_{22} is related to the number average ($\propto M$). Since this work deals with light scattering A_2, further references to B_{22} will be omitted.

If $A_2 > 0$, the net interparticle pair interactions are positive, which tends to stabilize the solution. $A_2 = 0$ corresponds to the ideal polymer case—that is, no interparticle interactions—such as at the theta temperature, whereas $A_2 < 0$ indicates a net interparticle attraction and greater potential for instability.

In the SLS method, the Zimm single-contact approximation is useful for determining M_w, A_2, and the z-average mean square radius of gyration, according to

$$\frac{Kc}{I_R} = \frac{1}{M_w}\left(1 + \frac{q^2\langle S^2\rangle_z}{3}\right) + 2A_2c. \tag{6}$$

Applicable for $\frac{q^2\langle S^2\rangle_z}{3} \ll 1$, where I_R is the absolute Rayleigh scattering ratio (cm^{-1}), c is the concentration of the solute in g cm^{-3}, and q is the magnitude of the scattering vector

$$q\left(cm^{-1}\right) = \frac{4\pi n_s}{\lambda_0}\sin\theta/2 \tag{7}$$

where n_s is the index of refraction of the solvent, $n_s = 1.333$ for water, λ_0 is the vacuum wavelength of the incident laser and the detection angle in the scattering plane, where $\theta = 90°$ for both light scattering instruments used here. K is an optical constant, given by vertically polarized incident light by

$$K = \frac{4\pi^2 n_s^2(\partial n/\partial c)^2}{\lambda_0^4 N_A} \tag{8}$$

where N_A is the Avogadro's number, and the differential index of refraction is $\frac{\partial n}{\partial c} = 0.189\ cm^3g^{-1}$ is typical for proteins, whereas $\frac{\partial n}{\partial c} \approx 0.150\ cm^3/g$ is typical for most polysaccharides, such as hyaluronate and alginate. I_R was obtained from the raw light scattering voltage with reference to toluene scattering of $I_R = 1.34 \times 10^{-5}\ cm^{-1}$ at $T = 25\ °C$ for $\lambda_0 = 640$ nm and $1.19 \times 10^{-5} cm^{-1}$ at 660 nm.

A_2 is determined in the low-angle limit ($q = 0$) by

$$\frac{Kc}{I_R} = \frac{1}{M_w} + 2A_2c + 3A_3c^2 + \ldots O\left(c^3\right) \tag{9}$$

where A_3 is the third virial coefficient, and $O\left(c^3\right)$ indicates terms in c^3 and higher powers. For the single-angle 90° measurement used in the SLS and DLS instruments here, it is important for $\frac{q^2\langle S^2\rangle_z}{3}$ to be negligible if M_w is to be determined, but, to first order, this restriction does not apply to determining A_2, which is angle independent in equation (6).

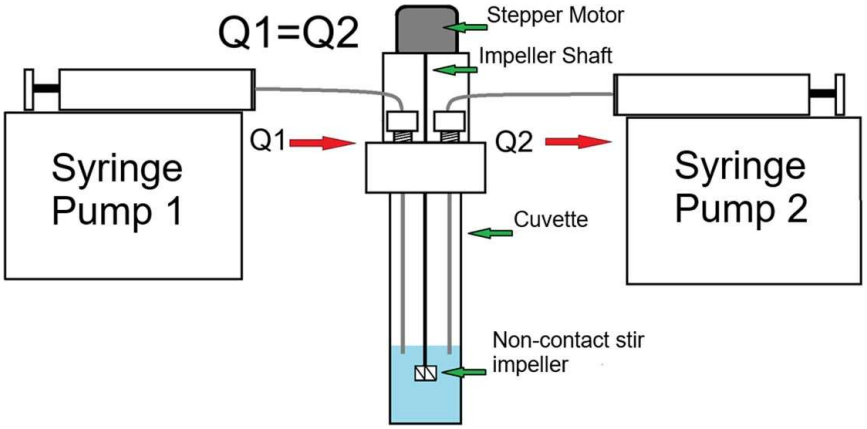
3.2. DLS

Brookhaven Instruments NanoBrook Omni (Holtsville, New York) was used for DLS and SLS. The photon count rate is proportional to intensity, and the rate was calibrated to the toluene count rate to convert to the Rayleigh scattering ratio I_R for the SLS measurement. $\lambda_o = 640$ nm was the vacuum wavelength of the vertically polarized incident light, the light scattering detection was at $\theta = 90°$, which gives the magnitude of the scattering vector:

$$q = 185{,}066 cm^{-1}. \tag{10}$$

The z-average mutual-diffusion coefficient, $<D_m>_z$, and polydispersity index, Q, were obtained by standard second-order cumulant analysis.

An important caveat in using DLS to disperse polymer and colloidal solutions, whose population includes particles for which $q^2\langle S^2\rangle_z \not\ll 1$, is that the measured diffusion coefficient, $<D_m>_z$, and polydispersity index, Q, depend on the value of q of the DLS instrument used. There is a variety of q-values among commercial DLS instruments because of their use of different laser wavelengths and detection



Scheme 1. Simplified schematic of the ACD apparatus.

angles, so that the values of $<D_m>_z$, and hence also k_D from equation (1) will vary among DLS instruments of different q. The reason is that scattering from larger particles decrease with increasing measurement angle θ, so that at finite angles, for example, 90°, the larger particles are underweighted, yielding a higher value of $<D_m>_z$ than would be obtained via extrapolation to $\theta = 0°$ [37]. Hence, based on fundamental principles, the values of $<D_m>_z$ will be different among DLS instruments with different values of q, and for disperse populations, there is no simple means of translating the results from one instrument to another without *a priori* knowledge of the size and mass distributions.

3.3. Standalone SLS

SLS measurements, to obtain only M_w and A_2, but at a much faster sampling rate (as high as 0.1 s, vs 120 s used in the DLS cycle) and higher sensitivity than the Brookhaven NanoBrook Omni, were made on a Fluence Analytics (now Yokogawa Fluence Analytics, Houston, Texas) Argen device, equipped with 16 independent sample cells, each with its own adjustable temperature, incident laser source at $\lambda_0 = 660$ nm and detection at $\lambda_o = 90°$. Since SLS is insensitive to convective effects that require stop flow for DLS measurements, it is possible to make continuous, uninterrupted SLS measurements with the Argen. This yields a more precise value of A_2 but does not provide k_D.

3.4. ACD

A simplified schematic of the ACD apparatus is shown in scheme 1. The automatic cuvette-based dilution method works as follows: the initial sample of biologics or other macromolecules at known concentrations is pipetted into a standard 1 cm cuvette. The volume is typically 0.8–2 ml, and is held constant throughout the dilution process. This is achieved by diluting the cuvette solution with the desired solvent via a pump delivering the solvent at a given flow rate (Q_1) and a second pump removing the liquid from the cuvette at exactly the same rate ($Q_2 = Q_1$). The noncontact stir in the cell, provided by an impeller in the solution driven by an overhead stepper motor, assures very rapid and complete mixing. "Noncontact stir" means that the impeller contacts only the solution, not any part of the cuvette. This is an important distinction because contact stir, for example, via a magnetic stir bar resting on the cuvette bottom, has been shown to severely damage biologics [38, 39]. The motor/impeller and feed/withdrawal ports are integrated into a cap assembly that fits directly into a standard 1 cm spectroscopic cuvette. This system and method can be used with any instrument accepting such standard cuvettes. The device is similar to the one used recently, but without the dialysis membrane [40].

The cuvette acts as a mixing chamber, such that the concentration of biologic or other macromolecules, in the cuvette, $c(t)$, is computed by

$$c(t) = c_0 e^{-\frac{Q}{V}t} \tag{11}$$

where c_0 is the initial concentration in the cuvette (g cm^{-3}), V (cm^3) is the constant volume in the cuvette and Q (cm^3 s^{-1}) is the flow rate from the solvent reservoir into the cuvette. Fluid is extracted from the cuvette with a separate pump, withdrawing at the same rate Q. For the measurements in this work, $V = 2$ cm^3 and $Q = 0.001$ cm^3 s^{-1} run for 2 hours. This gives a total of 4.6× final volume in the

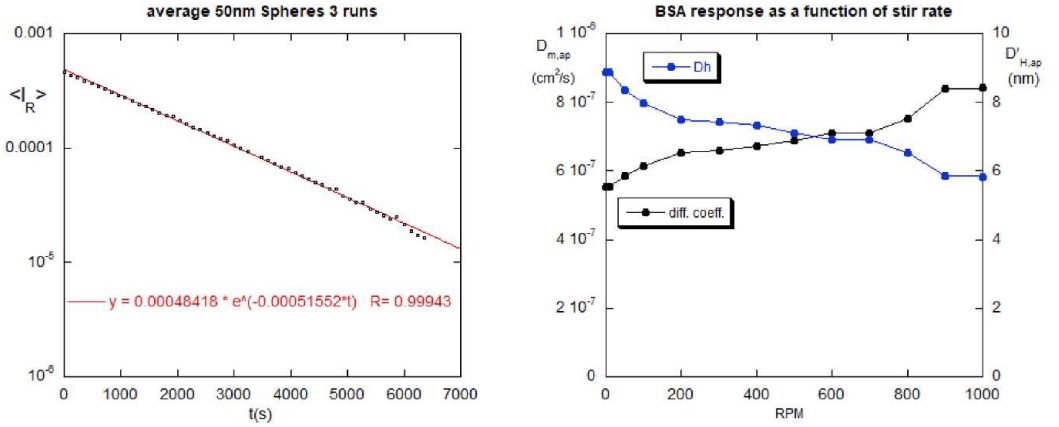


Figure 1. (a) Verification of equation (11). The average scattering from three independent runs of noninteracting spheres at the concentration of 5.0×10^{-5} g cm^{-3} was used. (b) The apparent mutual diffusion coefficient, $D_{\mathrm{m,ap}}$ vs stirring RPMs, showing the expected increase due to increasing convection. For convenience, the apparent, convection-impacted apparent hydrodynamic parameter $D'_{\mathrm{H,ap}}$ is also shown. The sample is BSA, at a concentration of 0.001 g cm^{-3}, in 100 mM aqueous NaCl.

withdrawal reservoir, that is about a 20% dilution of the initial sample concentration. With the current parameter, this leads to 9.2 ml in the withdrawal reservoir, making sample recovery straightforward.

Figure 1(a) verifies the accuracy of equation (11). Nominally, 51 nm latex spheres at very low dilution, 5×10^{-5} g cm^{-3}, were used so that A_2 effects are unmeasurably small, and the light scattering intensity is linear in concentration. Figure 1(a) shows the logarithmic light scattering intensity, I_{R}, vs t, where I_{R} was averaged over three runs. The linear fit is very close, with high correlation; therefore, equation (11) is used to compute $c(t)$ in all the following experiments.

When used with DLS, the hydrodynamic size range is approximately 1 nm to 10 μms. For SLS, the lower limit is approximately 0.001 g cm^{-3} for a 1000 g mol $^{-1}$ polymer. The upper limit is limited by the single 90° angle used here and requires $\frac{q^2\langle S^2\rangle_z}{3} \ll 1$. This corresponds to a root mean square radius of gyration of approximately 100 nm, whereas the mass depends on the morphology of the polymer or colloid, for example, random coils, rods, spheres, among others. This restriction is removed for multiangle light scattering, where extrapolation of q –> 0 can be made.

3.5. The problem of convective motion for DLS

DLS for determining k_{D} in this method involves measuring mutual diffusion coefficients, and their dependence on concentration, $D_{\mathrm{m}}(c)$. Convective motion of the solution, due to non-contact stirring, can be combined with the diffusional portion of the scattering intensity autocorrelation function, leading to erroneous measurements of $D_{\mathrm{m}}(c)$.

Most commercial autocorrelators, including the NanoBrook Omni, use homodyne detection, which means that the time-dependent intensity of the light scattered from the sample is autocorrelated directly, yielding the scattered intensity autocorrelation function $g_2(\tau)$ and does not mix with any portion of the incident beam. In the latter mixing case, heterodyne detection yields the scattered electric field autocorrelation function $g_1(\tau)$. In the homodyne detection mode, if the velocity $\vec{v}$ of all scatterers is exactly constant, then $g_1(\tau)$ is given by [41]:

$$g_1(\tau) = \mathrm{e}^{-D_{\mathrm{m}}q^2\tau}\mathrm{e}^{\mathrm{i}\vec{q}\cdot\vec{v}\tau} \tag{12}$$

where the complex exponential shows the effect of the convective motion on $g_1(\tau)$. Under the Gaussian assumption—the fact that the independent random phase shifts of scattered light from all the scatterers lead to a sum of electric fields, which is Gaussian distributed—$g_1(\tau)$ and $g_2(\tau)$ are related by

$$g_2(\tau) = 1 + \beta|g_1(\tau)|^2 \tag{13}$$

where β is a constant that depends primarily on the ratio of the coherence area of the DLS detector to the photoactive area of the detector. For completely constant $\vec{v}$, the effect of convection disappears in the

measured $g_2(\tau)$, when taking the complex conjugate in $|g_1(\tau)|^2$ in equation (12):

$$g_2(\tau) = 1 + \beta e^{-2D_m q^2 \tau}. \tag{14}$$

However, the convective motion no longer disappears in $g_2(\tau)$ if there is a distribution of velocities $P(\vec{v})$. In this case, $g_1(\tau)$ is averaged over all $\vec{v}$ in the velocity space:

$$g_1(\tau) = e^{-D_m q^2 \tau} \int P(\vec{v})\, e^{i\vec{q}\cdot\vec{v}\tau} d^3v = e^{-D_m q^2 \tau} F(\vec{q}, \tau) \tag{15}$$

where $F(\vec{q}, \tau)$ represents the integral in equation (15), which is the Fourier transform of $P(\vec{v})$ over the velocity space, and contains the effects of convection. Hence,

$$g_2(\tau) = 1 + \beta e^{-2D_m q^2 \tau} |F(\vec{q}, \tau)|^2. \tag{16}$$

Equation (16) shows the effect that convection has on when there is a distribution of velocities, $P(\vec{v})$, such as in stirred motion. For a sample stirred by a rotating shaft in the z-direction and detection in the scattering plane, which is perpendicular to this axis, the problem of computing $F(\vec{q}, \tau)$ is quite complex and will not generally yield a simple exponential, such as in equation (14). The analysis is beyond the scope of this work and not necessary to understand the implications of the stirring. Figure 1(b) shows the measured apparent mutual diffusion coefficient $D_{m,ap}$ for BSA, at a concentration of 0.001 g cm^{-3}, when the resulting intensity correlation under stir is force-fit to a simple exponential. $D_{m,ap}$ (cm^2 s^{-1}) increases by a factor of 53% going from 0 RPM to 1000 RPM. For convenience, the apparent hydrodynamic diameter $D'_{H,ap}$(nm) is also shown from the Stokes–Einstein for monodisperse spheres

$$D_0 = \frac{k_B T}{3\pi \eta D_H} \tag{17}$$

where D_H is the true hydrodynamic diameter of the monodisperse spheres, and $D'_{H,ap}$ includes the effect of both the convection and z-averaging

$$D'_{H,ap} = 1/\langle 1/D_H{}' \rangle_z \tag{18a}$$

where $D_H{}'$ is the convection-affected hydrodynamic diameter, obtained from the force-fit of the autocorrelation function to a single exponential *(Brackets, $< >$, indicate averaged values, throughout this work).*

The apparent hydrodynamic diameter, $D_{H,ap}$, is the zero-stir value extrapolated to $c = 0$ and is termed

$$D_{H,ap} = \lim_{c \to 0} 1/\langle 1/D_H \rangle_z \tag{18b}$$

and is the value cited in the results.

The (poly)dispersity index, Q, from the DLS autocorrelation function is the ratio of the second moment to the first moment squared of the cumulant expansion of the logarithm of the electric field autocorrelation function:

$$Q = \frac{\langle D_m^2 \rangle_z - \langle D_m \rangle_z^2}{\langle D_m \rangle_z{}^2}. \tag{19}$$

3.6. Stop-flow cycle for DLS

Since the convective effect distorts the determination of D_m, as just shown, the method here follows a cycle between measurements as continuous dilution occurs; (i) tens of seconds of rapid, efficient stirring with the noncontact impeller; (ii) a quiescent period of tens of seconds where the stirring is stopped; and (iii) subsequent DLS measurements on the quiescent solution for tens of seconds. An entire cycle is typically 2 min, although it can be shortened or lengthened. A typical cycle involves 20 s of stirring, 40 s of stopped stirring, and 60 s of DLS autocorrelation measurement. These periods can be flexibly modified by programming the stir motor and DLS data gathering software. The minimum amount of time to come to quiescence for a given stir rate was assessed by measuring DLS for a series of times and comparing them to a fully quiescent (never stirred) sample, to find where they converged.

4. Results and discussion

4.1. BSA

Figure 2(a) shows the averaged $<Kc/I_R>$ and $<D_{m,z}>$ results of three separate ACD runs for BSA in aqueous 100 mM NaCl, starting at a concentration of 0.060 g cm^{-3}. The error bars are the standard deviation of the three measurements at each point. The average $<M_w>$ = 67 600 is within 2% of the known value of 66 430 g mol^{-1}, whereas A_2 is within the expected order of $10^{-4}-10^{-5}$ cm$^3-$mol g^{-2} and depends on ionic strength, pH, and temperature. There is significant upwards curvature to $<Kc/I_R>$, such that $<A_3>$ can be computed by equation (9).

Since BSA is a globular protein, the hydrodynamic interactions are weak; therefore, a very slightly positive k_D is found. Small and negative k_D values have variously been reported for BSA, depending on conditions [42, 43].

Figure 2(b) shows continuous data during ACD measurements on the Argen instrument. The results compare favorably and are within the error bars of figure 2(a).

The relationship for hard spheres among A_2, molar mass M, and diameter d is given by

$$A_2 = \frac{2\pi d^3 N_A}{3M^2} \tag{20a}$$

and A_3 is related to A_2, generally, by

$$A_3 = \beta M A_2^2 \tag{20b}$$

where β is a dimensionless constant of order unity, whose value depends on the details of the polymer or colloid and its solution environment.

Using $d = D_{H,ap}$ = 9.06 nm, and M = 66 500 g mol $^{-1}$ in equation (20a) yields $A_{2,theoretical}$ = 2.12 $\times$ 10^{-4} cm$^3-$mol g^{-2}. The fact that the average measured A_2 = 8.45 $\times$ 10^{-5} cm$^3-$mol g^{-2} is about 40% of this value, suggesting that there are attractive surface patches on BSA that lower the net interaction energy below that of an equivalent hard sphere while still remaining net-repulsive. Other factors causing the deviation may include hydration layers, and some asphericity of BSA. By taking the average measured value of A_2 = 8.45 $\times$ 10^{-5} cm$^3-$mol g^{-2}, and computing an effective d in equation (20a) a yields d = 6.68 nm, compared to $D_{H,ap}$ = 9.06 nm, explicitly showing the reduction in effective diameter for BSA compared to a pure hard sphere. Using the experimental values of A_2 and A_3 in equation (20b) yields β = 1.47, which is a reasonable value for a protein.

4.2. Sodium hyaluronate (HA)

Figure 3 shows ACD data for the averages $<Kc/I_R>$ and $<D_{m,z}>$ for sodium hyaluronate (HA), a vital biomacromolecule used in a large number of pharmaceutical applications [44–46]. Although the single angle measurement at 90° is not sufficient to report an accurate M_w, it both establishes a lower bound for the latter. More importantly, it shows that A_2 and k_D are both positive. A_2 in the approximations of equations (6) and (9) is angle-independent. HA is a semi-rigid polyanion with persistence length around 10 nm at 150 mM NaCl [47]. Because of this, inter-HA interactions resemble the interactions of rigid rod segments, leading to repulsive hydrodynamic interactions, which, coupled with positive A_2, gives a large positive increase of $D_m(c)$ vs c [48, 49], and hence a large k_D. Positive increases in $D_m(c)$ vs c have also been found for other semirigid polyelectrolytes, such as xanthan [50, 51] and DNA [52, 53].

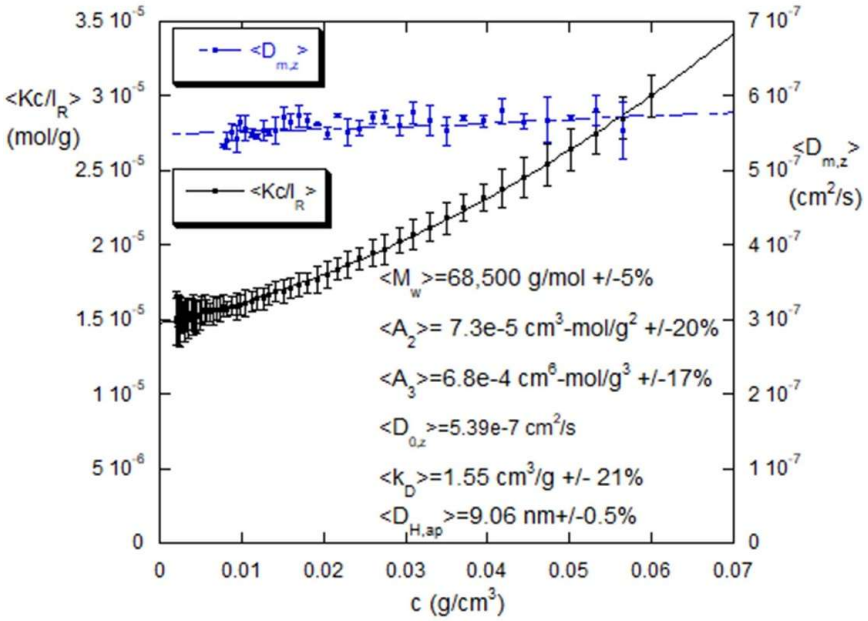
The data from figure 3 yield k_D = 372 cm^{-3} g, using the slope and intercept of $<D_{m,z}>$ vs concentration.

Using $<M_w>_{angle\text{-}corrected}$ = 1.01 $\times$ 10^6 $\pm$ 7% from table 2, where $<M_w>_{angle\text{-}corrected}$ = is given by $M_{w,cor}$ in equation (25), and the average $<A_2>$ for A_2 in equation (2) yields $k_H \sim -9800$ cm^3 g^{-1}. This is a physically meaningless high negative value under the spherical approximation, and simply illustrates that equation (2), only valid for dilute spheres, is conceptually mismatched to the case of a large, semi-rigid random coil with coil interpenetration.

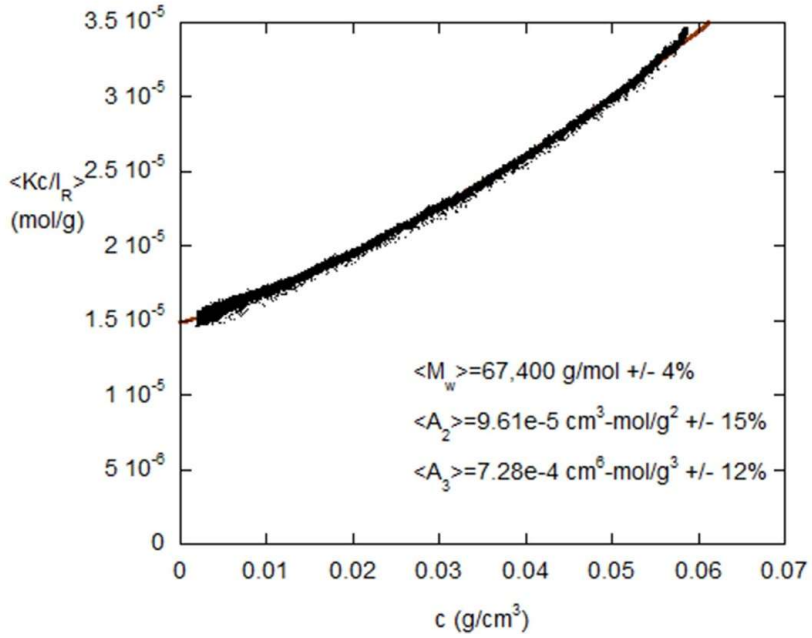
It is reminded that HA is a large, highly charged polyanion; therefore, all values, except M_w, are strongly dependent on ionic strength, which for figure 3 is 100 mM. A_2 increases as ionic strength decreases from this value, while $<D_{0,z}>$ decreases, and k_D increases.

4.3. Alginate

Figure 4 shows ACD data averaged over three separate runs, $<Kc/I_R>$ and $<D_{m,z}>$ for alginate, a naturally occurring polyanion. A_2 = 7.3 $\times$ 10^{-4} cm$^3-$mol g^{-2}, which shows a strong repulsion between the



(a)



(b)

Figure 2. (a) $<Kc/I_R>$ and $<D_{m,z}>$ vs c for BSA in aqueous 100 mM NaCl, using the Brookhaven NanoBrook Omni. (b) $<Kc/I_R>$ vs c for BSA in aqueous 100 mM NaCl, using SLS from the Argen instrument. This instrument has higher sensitivity than the Brookhaven NanoBrook Omni, and data can be gathered continuously, without the stop-flow cycle required for DLS.

negatively charged chains. In contrast, k_D is strongly negative, with $D_m(c)$ showing a scaling law of

$$\langle D_{m,z}(c)\rangle = 7.34x10^{-10}c^{-0.43} \tag{21}$$

This is actually a classical result for semi-dilute solutions of flexible polymers, first predicted by De Gennes [54], confirmed theoretically [55, 56] and experimentally [57, 58].

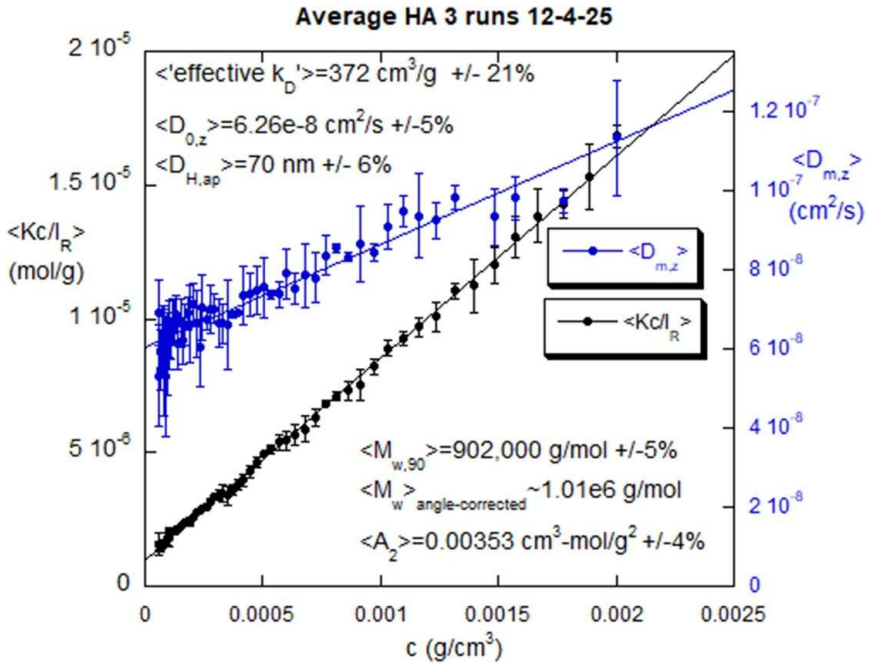


Figure 3. The average values, $<Kc/I_R>$ and $<D_{m,z}>$, from three independent runs for HA in aqueous 150 mM NaCl. Kc/I_R. The average values for $<M_{w,90}>$, the angle-corrected value $<M_w>_{angle\text{-}corrected}$, $<Q_2/>$, <'effective k_D'>, $<D_{0,z}>$, and the average apparent hydrodynamic diameter $<D_{H,ap}>$ computed from $<D_{0,z}>$.

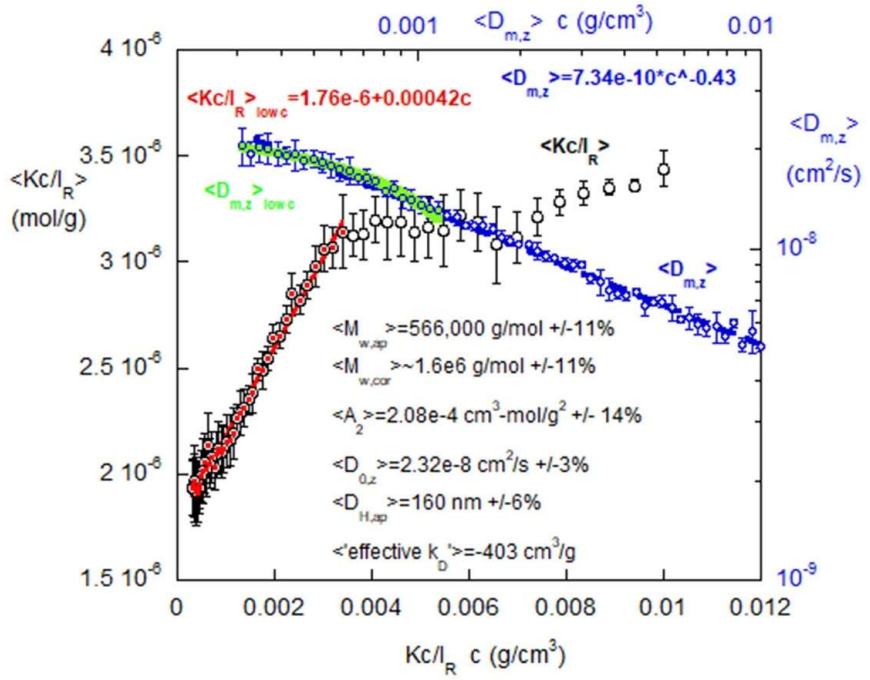


Figure 4. The average values, $<Kc/I_R>$ and $<D_{m,z}>$, from three independent runs for alginate in aqueous 100 mM NaCl. Kc/I_R. The large, negative k_D shows that there are chain overlap and entanglement effects, such that equation (2) is not applicable. The red data points are the linear region of $<Kc/I_R>$ from which $<Q_2/>$ and $<M_{w,ap}>$ are determined.

Further evidence demonstrates that the semidilute regime is reached in figure 4 can be seen in the way Kc/I_R flattens out as concentration increases. Normally, in the dilute regime, with no chain overlaps, positive A_3 effects would occur at higher concentration, causing Kc/I_R to have a positive second derivative (upward curvature). The flattening is most likely due to transient, small clusters forming as

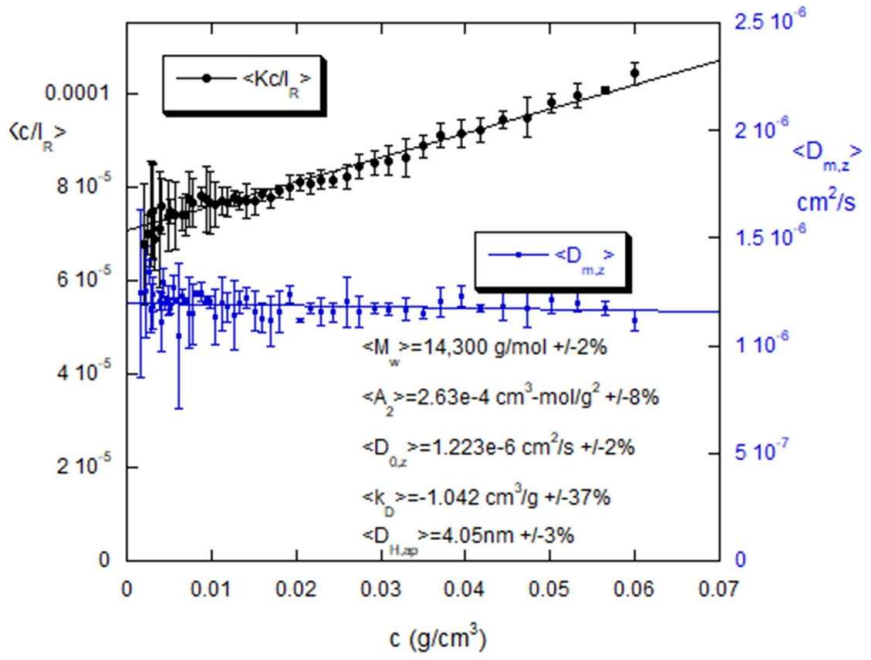


Figure 5. Determination of $<M_w>$, $<Q_2/>$, and $<k_D>$, etc, for lysozyme, in 100 mM aqueous NaCl.

concentration increases. Alginate is known to self-associate as ionic strength increases even with monovalent salts [59, 60], and forms complex "egg-box" association with divalent ions [61]. Further evidence of this is shown in figure 8, where the polydispersity index Q increases vs concentration, opposite to the other three macromolecules, indicating increased polydispersity in size due to clustering.

4.4. Lysozyme

Figure 5 shows M_w falls on the known value of 14 300 g mol^{-1} for lysozyme. $A_2 = 2.63 \times 10^{-4}$cm^3 −mol g^{-2} is strongly positive. In contrast to BSA, M_w is too small over the concentration range for an A_3 to be measurable. The computation of A_2 by equation (20*a*), using $d = <D_{H,ap}> = 4.05$ nm yields $A_{2,theoretical} = 4.09 \times 10^{-4}$cm^3−mol g^{-2}. The fact that the average measured $A_2 = 2.63 \times 10^{-4}$ cm^3−mol g^{-2} is 64% of this value suggests that, similar to the BSA results above, there are attractive surface patches on lysozyme that lower the net interaction energy below that of an equivalent hard sphere while still remaining net-repulsive. The attractive interaction effect is less for Lysozyme than for BSA, with BSA A_2 at 40% of the average measured value, and 64% for that of Lysozyme. Computing an effective d in equation (20*a*) yields $d = 3.5$ nm, compared to $D_{H,ap} = 4.05$ nm, making explicit the lower effective diameter of lysozyme compared to a hard sphere.

4.5. Latex nanosphere size standards

Figure 6 shows there is no measurable concentration dependence for $<D_{m,z}>$ for the latex spheres so that k_D is unmeasurably small. Likewise, since the concentration range of the measurements was so low ($\sim$5.0 $\times$ 10^{-5}g cm^{-3}), the concentration dependence of $<Kc/I_R>$ is not discernible and can have a slightly positive or negative value, depending on how the points are weighted. Hence, $A_2 \sim 0$.

Using equation (20*a*) for hard spheres with $d = 5.71 \times 10^{-6}$cm and $M = 8.47 \times 10^7$ g mol^{-1} yields a very small theoretical $A_{2,theoretical} = 2.96 \times 10^{-8}$ cm^3−mol g^{-2}. At the highest concentration of 2.5 $\times$ 10^{-5}g cm^{-3}, $2A_{2,theoretical}M_w c = 1.32 \times 10^{-4}$; that is, at the highest concentration, the A_2 term in equation (9) is only 0.013% of the M_w term. This is unmeasurably small, and the lack of a significant A_2 term justifies the use of the spheres in verifying the validity of equation (11).

4.6. Error comparison among samples

The error bars shown in the above figures are based on standard deviations obtained over three independent experiments. The size of the error bars varies noticeably among the samples, and seems to be related to the sample's "quality". One means of comparing the errors is to find the concentration of each sample at which I_R has a set comparison value, $I_{R,comp}$, and then lists the corresponding error bars. Here,

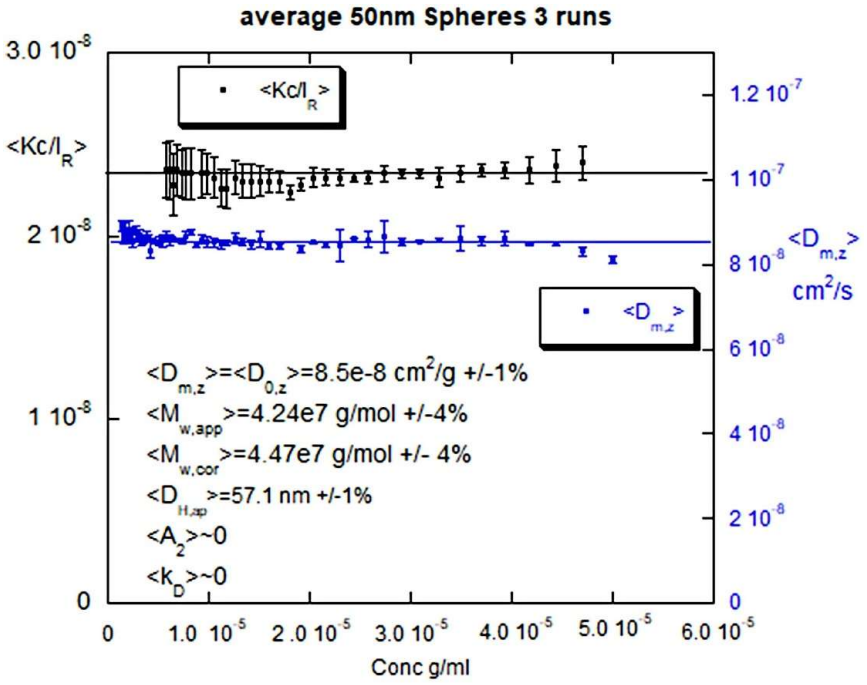


Figure 6. $<Kc/I_R>$ and $<D_{m,z}>$ for the nominal 51 nm nanosphere size standards in salt-free water. Error bars are the standard deviation from three independent ACD measurements.

Table 1. Comparison of error bars among samples.

Sample	dn/dc (cm^3 g^{-1})	K	M_w (g mol^{-1})	c_{comp}@ I_R $= 1 \times 10^{-4}$	%error $<Kc/I_R>$ @$I_R = 1 \times 10^{-4}$	Known M_w (g mol^{-1})
BSA	0.185	2.09×10^{-07}	66 500	7.20×10^{-03}	3.4	66 430
HA	0.15	1.37×10^{-07}	1.10E + 06	6.62×10^{-04}	8.4	Varies
Alginate	0.15	1.37×10^{-07}	1.60E + 06	4.55×10^{-04}	10.2	Varies
Lysozyme	0.185	2.09×10^{-07}	14 300	3.35×10^{-02}	2.6	14 300
Latex spheres	0.185	1.76×10^{-07}	~4.470E + 07	6.44×10^{-06}	1.6	~4.40×10^7

a convenient value is $I_{R,comp} = 10^{-4}$ cm^{-1}, which is roughly 10× the value of toluene scattering. The concentration for comparison c_{comp} is found from

$$c_{comp} = \frac{I_{R,comp}}{KM_w} \tag{22}$$

and is shown in table 1, along with each sample's dn/dc, K, and M_w. The % error at this concentration is the rightmost column in table 1.

The lowest error, 1.6%, is for the latex spheres, and the highest, 10.2%, is for the alginate. This suggests that the latex sphere error is close to the natural error bar of the Brookhaven DLS (the count rate for each measurement was converted to I_R in the figures) at $I_{R,comp}$, and that the other error bars, which are higher, are attributed to the inherent complexities of biological macromolecules. Nonetheless, the error bars for BSA and Lysozyme, 3.4% and 2.6%, respectively, are low, as might be expected for nominally monodisperse globular proteins. In contrast, the higher error bars of the polysaccharides, 8.4% and 10.2%, for HA and alginate, respectively, reflect the significantly higher heterogeneity of these samples.

4.7. Influence of the A_2 and A_3 terms in equation (9)

Figure 7 shows the ratio of the A_2 and A_3 terms in equation (9) to the leading $1/M_w$ term, which is the dimensionless quantity $2A_2M_wc + 3A_3M_wc^2$:

$$\frac{A_2 \text{ and } A_3 \text{ term in Eq. 9}}{\frac{1}{M_w}\text{term in Eq. 9}} = 2A_2M_wc + 3A_3M_wc^2. \tag{23}$$

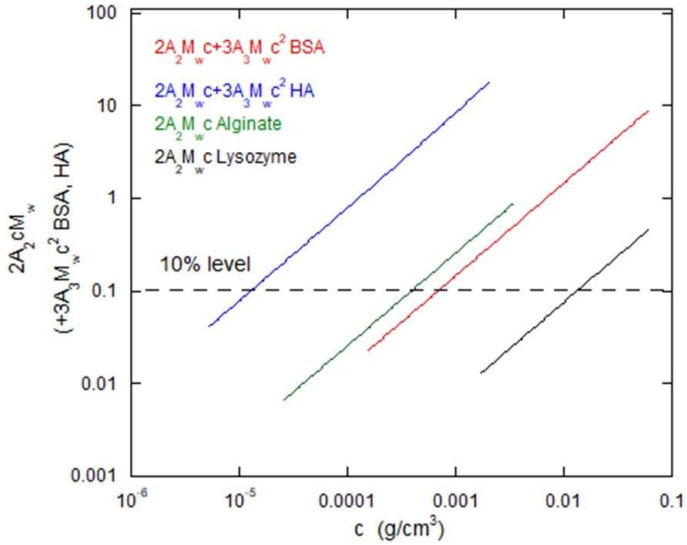


Figure 7. The dimensionless $2A_2M_wc + 3A_3M_wc^2$ term vs c for the four biomacromolecules investigated. Only BSA had a measurable A_3 term, so that the other macromolecules only involve. $2A_2M_{wc}$.

Table 2. Summary of macromolecular characteristics from ACD measurements.

	BSA	HA	Alginate	Lysozyme	57 nm spheres
$<M_{w,ap}>$ (g mol^{-1})	68 500 ± 5%	902 000 +/7%	566 000 ± 11%	14 300 ± 2%	8.47×10^7 ± 2%
$<M_{w,cor}>$ (g mol^{-1})	68 600 ± 5%	1.01×10^6 ± 7%	1.60×10^6 ± 11%	14 300 ± 2%	8.94×10^7 +/2%
$<A_2/>$ (cm^3−mol g^{-2})	7.3×10^{-5} ± 20%	3.53×10^{-3} ± 4%	2.08×10^{-4} +/14%	2.63×10^{-4} ± 8%	∼0
$<A_3/>$ (cm^6-mol g^{-3})	6.8×10^{-4} ± 17%	NM	NM	NM	NM
$<D_0>_z$ (cm^2 s^{-1})	5.39×10^{-7} ± 2%	6.26×10^{-8} ± 5%	2.21×10^{-8} ± 3%	1.22×10^{-6} ± 2%	8.58×10^{-8} ± 1%
$<D_{H,ap}>$ (nm)	9.06 ±0.5%	70.0 ±6%	169 ± 6%	4.05 ±3%	57.1 nm ±1%
d (nm) from A_2	6.48 ±3%	NA	NA	3.5 ±2%	∼47 nm
$<k_D>$ (cm^3 g^{-1})	1.55 ± 21%	NA	NA	1.04 ±37%	∼0
<'effective k_D'> (cm^3 g^{-1})	NA	372 ± 21%	−342 ± 8%	NA	NA

NM = not measurable.
NA = not applicable.

This represents the light scattering relationship between the A_2 (two body) plus A_3 (three body) interactions and the single-molecule value, M_w. The values used in the computations for figure 7 are the average values $<M_w>$, $<A_2>$ and $<A_3>$ (the latter for BSA only) from the ACD results in table 2. Only BSA and HA had measurable A_3 terms over the concentration ranges used, so the other macromolecule results in figure 7 involve only $2A_2cM_w$. The values of $2A_2M_wc + 3A_3M_wc^2$ are shown over the range of concentration measured for each macromolecule. The term for alginate has been cut off for concentrations above 0.0033 g cm^{-3}, as above that it begins to enter the semidilute chain overlap regime where the virial expansion of equation (9) no longer holds.

Figure 7 shows that at their highest concentration the virial terms are 18× and 9× greater than the M_w term for HA and BSA, respectively, and 2.5× and 0.45× for alginate and lysozyme, respectively. Below the dashed line in figure 7, the sum of the virial coefficient terms is less than 10% of the M_w term. At the lowest concentration for each, the virial sums are as follows: HA 4%, alginate 0.6%, BSA 2%, and lysozyme 1.2%. Since the data are extrapolated to $c = 0$, only angular corrections for HA and alginate are needed. A procedure for estimating the angular correction is given below.

4.8. Polydispersity behavior

Figure 8 shows the (poly)dispersity parameter Q, defined in equation (19), and obtained from the linear and quadratic terms of the logarithmic autocorrelation expansion in the delay time τ.

For HA and lysozyme Q increases as concentration decreases. This may be due to one or more mechanisms; i) In a broad polymer population where $A_2 \propto M^{-0.2}$ the virial term is $2A_2Mc \propto M^{0.8}c$. This means that the larger the M, the larger its contribution to the virial term. As concentration decreases,

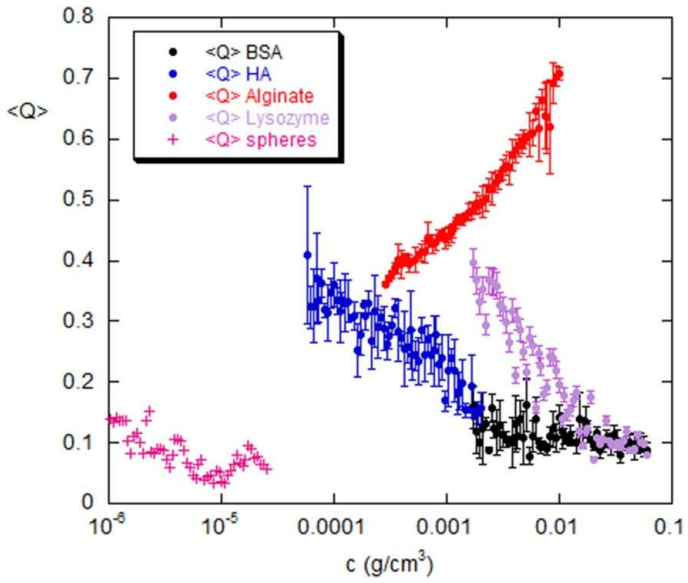


Figure 8. $<Q>$ vs c for all the samples.

the A_2 suppression of scattering at larger M decreases, making their scattering more prominent while decreasing $D_{m,z}$ and increasing polydispersity Q. ii) Even in low dispersity populations, if there is a small, stable population of large impurities, such as aggregates, entanglements, or "dust," each particle produces a spike as it transits the scattering volume, which perturbs the autocorrelation function away from a single exponential; that is, increases Q. Upon dilution, the perturbing effect of these particles becomes larger as the polymer signal decreases, even though they transit the scattering volume less frequently as they are diluted. iii) As dilution continues, there is some chance of scattering impurities becoming more numerous due to possible sloughing off from the noncontact stir impeller and possibly from the dilution solvent even though this enters the cuvette via a 0.22 μm filter on the outlet of the syringe pump feeding the cuvette.

In light of these effects, for HA, the most plausible cause of Q increase upon dilution is i), the virial effect on a highly dispersed population upon dilution. For lysozyme, i) does not apply and explanation ii) and/or iii) is most probable. For BSA and spheres, there is only a small increase in Q upon dilution so that either ii) or iii) are plausible. Mechanism i), based on virial effects, only applies to HA.

In contrast, Q for alginate decreases with decreasing concentration. This reinforces the finding in figure 4: Kc/I_R vs c flattens out at higher concentrations, rather than becoming concave upward, due to the formation of clusters in the semidilute regime. $<D_{m,z}>$ decreases with increasing concentration due to the formation of the larger, more slowly diffusing clusters. The increasing polydispersity for alginate in figure 8 shows the size distribution widening as clusters are formed.

4.9. Angular correction to M_w; $M_{w,angle\text{-}corrected}$ ($M_{w,cor}$)

Although the determination of M_w is not the principal aim of this work, it can nonetheless be accurately determined when $\frac{q^2\langle S^2\rangle_z}{3} \ll 1$. Single-angle measurements were used (90°) so that if this latter condition does not hold, then M_w underestimates the true M_w, normally found by a multiangle extrapolation to $\theta = 0$. The angle-corrected M_w, $M_{w,cor}$, can be estimated from the value of I_R/Kc ($=M_{w,90}$) extrapolated $c = 0$ value obtained from the concentration dependent Kc/I_R data. The relation between the root mean square radius of gyration $\langle S^2\rangle_z^{1/2}$ and the hydrodynamic diameter for an ideal random coil is

$$\langle S^2\rangle_z^{1/2} = 0.75 D_H \tag{24a}$$

whereas, for a solid sphere of uniform density

$$\langle S^2\rangle_z^{1/2} = \frac{1}{2}\sqrt{\frac{3}{5}} D_H. \tag{24b}$$

Approximating $D_{\mathrm{H}} \approx D_{H,\mathrm{ap}}$ from the extrapolation to $c = 0$, the angle-dependent term in equation (6) is

$$\frac{M_{\mathrm{w,cor}}}{M_{\mathrm{w,90}}} \approx \left(1 + \frac{q^2\langle S^2\rangle_z}{3}\right). \tag{25}$$

Using the hard sphere equation (24*b*) for BSA and lysozyme and the random coil equation (24*a*) for HA and alginate in Equation yields the $M_{\mathrm{w,cor}}$ given in table 2.

4.10. Tabulated data

Table 2 collects the data on all samples, for ready summary and comparison.

5. Summary

Cuvette-based ACD is shown to be a rapid, efficient means of simultaneously determining M_{w}, A_2 (and A_3 at high enough concentrations), $D_{\mathrm{H,ap}}$, polydispersity Q (equation (19)), and k_{D}, with a relatively small number of samples. The sample can also be recovered, if desired, from the final diluted cuvette output reservoir, which is typically diluted 5× from initial sample concentration, yielding about 10 ml of fully diluted sample for recovery, with the ACD flow rate and volume parameters used here.

Full ACD measurements can typically be completed in about 1 h, and no sample beyond the initial amount at the highest concentration is required. The accuracy of the method benefits from the fact that the cuvette, incident laser, and detector remain fixed throughout the experiment while maintaining constant optical geometry. In addition, the continuous dilution trajectory eliminates the need to prepare and measure multiple discrete samples, reducing sample consumption and simplifying the experimental workflow. Since the measurement is performed entirely within a single cuvette, the diluted sample can also be readily recovered after the experiment if desired.

The relationship between A_2, the diffusive hydrodynamic parameter k_{H} (from equation (2)) and k_{D} is discussed as well as the fact that these parameters do not quantitatively predict formulation viscosity, η, even at low concentrations of biologic material. However, since both k_{D} and η are related to hydrodynamics, albeit in very distinct ways, k_{D} can be useful as an empirical screening for the risk of unwanted high viscosity behavior of biologics at high concentration. Direct measurement of high concentration viscosity is usually impractical due to the quantity of biologic material needed and possible artifacts in measurements.

The results are shown for three important paradigms: i) the case where strong repulsive thermodynamic and hydrodynamic interactions lead to positive A_2 and "effective k_{D}" (HA), ii) where A_2 is positive and strong, yet "effective k_{D}" is negative and strong due to polymer coil overlap, chain entanglement, and the resulting hydrodynamic drag (alginate), and iii) A_2 is positive, whereas k_{D} is very small for globular proteins, such as BSA and lysozyme.

The random errors among the samples are compared and show that the latex spheres are closest to the instrument precision, whereas the globular proteins (BSA and lysozyme) are only slightly above this, whereas the polysaccharides (HA and alginate) have much greater error bars, reflecting the inherent inhomogeneity of these coil-like biomacromolecules.

A_2 is an important parameter for colloidal stability of biologic formulations—the higher A_2 is generally more stable the solutions—whereas the higher k_{D} the more likely that high concentration formulations will have relatively low viscosity, which is desirable for parenteral injection of mAbs and other biologics.

Beyond light scattering applications, since the method uses a standard 1 cm spectroscopic cuvette, ACD measurements can be made directly on any spectroscopic instrument accepting such cuvettes, without any modification to the instrument. This can include monitoring fluorescence, circular dichroism, UV/visible absorbance, and Raman, as samples are diluted, leading to changes in association states, solvochromaticity effects, and others.

Furthermore, two input reservoirs can be used, one containing the sample at twice the initial concentration of the sample in the cuvette, the other with a desired solvent or solvent plus excipient, whereas withdrawal occurs at twice the input flow rate. This maintains both volume and sample concentration constant in the cuvette. This method is termed "automatic continuous mixing" and can be useful, for example, in mapping the behavior of the sample as pH changes continuously. The pH (and electrical conductivity) of the cuvette can be directly monitored inside the cuvette, using an ion selective field effect transistor, as was previously demonstrated for a cognate cuvette-based dialysis monitoring method

[62]. It is also noted that the method is complementary to the cuvette platform's dialysis-based buffer exchange apparatus and method [40].

Acknowledgments

The authors acknowledge support from PolyRMC at Tulane University, the Murchison-Mallory Fund at Tulane University, and the Louisiana Board of Regents Endowed Professorship program.

Data availability statement

All data that support the findings of this study are included within the article (and any supplementary files).

ORCID iDs

Curtis W Jarand 0000-0002-7914-6699
Wayne F Reed 0000-0001-5821-3007

References

[1] Lehermayr C, Mahler H-C, Mäder K and Fischer S 2011 Assessment of net charge and protein-protein interactions of different monoclonal antibodies *J. Pharm. Sci.* **100** 2551–62
[2] Sorret L L, DeWinter M A, Schwartz D K and Randolph T W 2016 Challenges in predicting protein-protein interactions from measurements of molecular diffusivity *Biophys. J.* **111** 1831–42
[3] Roberts C J 2014 Therapeutic protein aggregation: mechanisms, design, and control *Trends Biotechnol.* **32** 372–80
[4] Strelitzki R and Reed W F 1999 Automated batch characterization of polymer solutions by static light scattering and viscometry *J. Appl. Polym. Sci.* **73** 2359–67
[5] Sorci G A and Reed W F 2002 Electrostatic and association phenomena in aggregates of polymers and micelles *Langmuir* **18** 353–64
[6] Sorci G A and Reed W F 2002 Electrostatically enhanced second and third virial coefficients, viscosity, and interparticle correlations for linear polyelectrolytes *Macromolecules* **35** 5218–27
[7] Attri A K and Minton A P 2005 Composition gradient static light scattering: a new technique for rapid detection and quantitative characterization of reversible macromolecular hetero-associations in solution *Anal. Biochem.* **346** 346132–8
[8] Fernández C and Minton A P 2008 Automated measurement of the static light scattering of macromolecular solutions over a broad range of concentrations *Anal. Biochem.* **381** 254–7
[9] Some D 2013 Some D 2013 Light-scattering-based analysis of biomolecular interactions *Biophys. Rev.* **5** 147–58
[10] Ferreon J C, Kongchan N, Tsoi P S, Choi K-J, Kenrick S, Neilson J and Ferreon A C M 2024 Multivalent protein–nucleic acid interactions probed by composition-gradient multiangle light scattering *ACS Omega* **9** 41003–10
[11] Kim S and Karrila S 2013 *Microhydrodynamics* (Elsevier)
[12] Happel J and Brenner H 1965 *Low Reynolds Number Hydrodynamics* vol 28 (Cambridge University Press)
[13] Doi M and Edwards S F 1988 *The Theory of Polymer Dynamics* (Oxford University Press)
[14] Yearley E J *et al* 2014 Observation of small cluster formation in concentrated monoclonal antibody solutions and its implications to solution viscosity *Biophys. J.* **106** 1763–70
[15] Douglas J F, Curtis R, S Sarangapani P, D Hudson S, L Jones R and A Pathak J 2017 Hard spheres with purely repulsive interactions have positive diffusion interaction parameter, kD *Biophys. J.* **113** 113753–4
[16] Yadav S, Shire S J and Kalonia D S 2012 Viscosity behavior of high-concentration monoclonal antibody solutions: correlation with interaction parameter and electroviscous effects *J. Pharm. Sci.* **101** 998–1011
[17] Yadav S, Liu J, Shire S J and Kalonia D S 2010 Specific interactions in high concentration antibody solutions resulting in high viscosity *J. Pharm. Sci.* **99** 1152–68
[18] Yadav S, Shire S J and Kalonia D S 2011 Viscosity analysis of high concentration bovine serum albumin aqueous solutions *Pharm. Res.* **28** 1973–83
[19] Connolly B D, Petry C, Yadav S, Demeule B, Ciaccio N, Moore J R, Shire S and Gokarn Y 2012 Weak interactions govern the viscosity of concentrated antibody solutions: high-throughput analysis using the diffusion interaction parameter *Biophys. J.* **103** 69–78
[20] Dauer K, Pfeiffer-Marek S, Kamm W and Wagner K G 2021 Microwell plate-based dynamic light scattering as a high-throughput characterization tool in biopharmaceutical development *Pharmaceutics* **13** 172
[21] Chen W-H *et al* 2017 Optimization of the production process and characterization of the yeast-expressed SARS-CoV recombinant receptor-binding domain (RBD219-N1), a SARS vaccine candidate *J. Pharm. Sci.* **106** 1961–70
[22] Tomar D S, Singh S K, Li L, Broulidakis M P and Kumar S 2018 In silico prediction of diffusion interaction parameter (kD), a key indicator of antibody solution behaviors *Pharm. Res.* **35** 193
[23] Kingsbury J S *et al* 2020 A single molecular descriptor to predict solution behavior of therapeutic antibodies *Sci. Adv.* **6** eabb0372
[24] Thakkar S V, Allegre K M, Joshi S B, Volkin D B and Middaugh C R 2012 An application of ultraviolet spectroscopy to study interactions in proteins solutions at high concentrations *J. Pharm. Sci.* **101** 3051–61
[25] Yu M, Silva T C, van Opstal A, Romeijn S, Every H A, Jiskoot W, Witkamp G-J and Ottens M 2019 The investigation of protein diffusion via H-cell microfluidics *Biophys. J.* **116** 116595–609

[26] Mach H and Middaugh C R 2011 Ultraviolet spectroscopy as a tool in therapeutic protein development *J. Pharm. Sci.* **100** 1214–27
[27] Schermeyer M-T, Wöll A K, Kokke B, Eppink M and Hubbuch J 2017 Characterization of highly concentrated antibody solution—a toolbox for the description of protein long-term solution stability *MAbs* **9** 1169–85
[28] Pindrus M, Shire S J, Kelley R F, Demeule B, Wong R, Xu Y and Yadav S 2015 Solubility challenges in high concentration monoclonal antibody formulations: relationship with amino acid sequence and intermolecular interactions *Mol. Pharm.* **12** 3896–907
[29] Moon Y U, Anderson C O, Blanch H W and Prausnitz J M 2000 Osmotic pressures and second virial coefficients for aqueous saline solutions of lysozyme *Fluid Phase Equilib.* **168** 229–39
[30] Deszczynski M, Harding S E and Winzor D J 2006 Negative second virial coefficients as predictors of protein crystal growth: evidence from sedimentation equilibrium studies that refutes the designation of those light scattering parameters as osmotic virial coefficients *Biophys. Chem.* **120** 106–13
[31] Mrozowich T, Winzor D J, Scott D J and Patel T R 2019 Experimental determination of second virial coefficients by small-angle x-ray scattering: a problem revisited *Eur. Biophys. J.* **48** 781–7
[32] Velev O D, Kaler E W and Lenhoff A M 1998 Protein interactions in solution characterized by light and neutron scattering: comparison of lysozyme and chymotrypsinogen *Biophys. J.* **75** 2682–97
[33] Latunde-dada S, Bott R, Barker D and Leszczyszyn O I 2015 Methodologies for the rapid determination of the diffusion interaction parameter using Taylor dispersion analysis *Anal. Methods* **8** 386–92
[34] Høgstedt U B, Schwach G, van de Weert M, Østergaard J and van de Weert M 2016 Taylor Dispersion Analysis as a promising tool for assessment of peptide-peptide interactions *Eur. J. Pharm. Sci.* **93** 21–28
[35] Kusova A M, Sitnitsky A E, Faizullin D A and Zuev Y F 2019 Protein translational diffusion and intermolecular interactions of globular and intrinsically unstructured proteins *J. Phys. Chem. A* **123** 12310190–6
[36] Yuriy Z *et al* 2023 Protein translational diffusion as a way to detect intermolecular interactions *Biophys. Rev.* **15** 1111–25
[37] Jin L, Jarand C W, Brader M L and Reed W F 2022 Angle-dependent effects in DLS measurements of polydisperse particles *Meas. Sci. Technol.* **33** 045202
[38] Drenski M, Brader M and Reed W 2015 Simultaneous multiple sample light scattering (SMSLS) for continuous monitoring of protein aggregation *ACS Symp. Series* pp 159–88
[39] Jarand C W and Reed W F 2018 On the reproducibility of early-stage thermally induced and contact-stir-induced protein aggregation *J. Phys. Chem. B* **122** 1229361–72
[40] Jarand C W, McLeod M J and Reed W F 2024 Dialysis monitoring of ionic strength and denaturant effects, and their reversibility, for various classes of macromolecules *Biomacromolecules* **25** 5198–211
[41] Berne J and Pecora R 1976 *Dynamic Light Scattering* vol 9 (Wiley)
[42] Jachimska B, Wasilewska M and Adamczyk Z 2008 Characterization of globular protein solutions by dynamic light scattering, electrophoretic mobility, and viscosity measurements *Langmuir* **24** 6866–72
[43] Ando T and Skolnick J 2010 Crowding and hydrodynamic interactions likely dominate *in vivo* macromolecular motion *Proc. Natl Acad. Sci. USA* **107** 18457–62
[44] Gupta R C, Lall R, Srivastava A and Sinha A 2019 Hyaluronic acid: molecular mechanisms and therapeutic trajectory *Front. Vet. Sci.* **6** 192
[45] Kotla N G, Bonam S R, Rasala S, Wankar J, Bohara R A, Bayry J, Rochev Y and Pandit A 2021 Recent advances and prospects of hyaluronan as a multifunctional therapeutic system *J. Control. Release* **336** 336598–620
[46] Yasin A, Ren Y, Li J, Sheng Y, Cao C and Zhang K 2022 Advances in hyaluronic acid for biomedical applications *Front. Bioeng. Biotechnol.* **10** 910290
[47] Morfin I, Buhler E, Cousin F, Grillo I and Boué F 2011 Rodlike complexes of a polyelectrolyte (hyaluronan) and a protein (lysozyme) observed by SANS *Biomacromolecules* **12** 859–70
[48] Ghosh S, Li X, Reed C and Reed W 1990 Apparent persistence lengths and diffusion behavior of high molecular weight hyaluronate *Biopolymers* **30** 1101–12
[49] Gribbon P, Heng B C and Hardingham T E 1999 The molecular basis of the solution properties of hyaluronan investigated by confocal fluorescence recovery after photobleaching *Biophys. J.* **77** 772210–6
[50] Milas M, Reed W F and Printz S 1996 Conformations and flexibility of native and re-natured xanthan in aqueous solutions *Int. J. Biol. Macromol.* **18** 211–21
[51] Jamieson A M, Southwick J G and Blackwell J 1982 Dynamical behavior of xanthan polysaccharide in solution *J. Polym. Sci. Polym. Phys. Ed.* **20** 1513–24
[52] Liu H, Skibinska L, Gapinski J, Patkowski A, Fischer E and Pecora R 1998 Effect of electrostatic interactions on the structure and dynamics of a model polyelectrolyte. I. Diffusion *J. Chem. Phys.* **109** 7556–66
[53] Wilk A, Gapinski J, Patkowski A and Pecora R 2004 Self-diffusion in solutions of a 20 base pair oligonucleotide: effects of concentration and ionic strength *J. Chem. Phys.* **121** 10794–802
[54] De Gennes PG 1979 *Scaling Concepts in Polymer Physics* (Cornell University Press)
[55] Rubinstein M and Colby R H 2003 *Polymer Physics* (Oxford University Press)
[56] Brown W 1993 *Dynamic Light Scattering: The Method and Some Applications* (Oxford University Press)
[57] Oono Y, Baldwin P R and Ohta T 1984 Cooperative diffusion constant of semidilute polymer solutions *Phys. Rev. Lett.* **53** 2149–52
[58] Klein J 1978 The onset of entangled behavior in semidilute and concentrated polymer solutions *Macromolecules* **11** 852–8
[59] Andriamanantoanina H and Rinaudo M 2010 Relationship between the molecular structure of alginates and their gelation in acidic conditions *Polym. Int.* **59** 1531–41
[60] Karakasyan C, Legros M, Lack S, Brunel F, Maingault P, Ducouret G and Hourdet D 2010 Cold gelation of alginates induced by monovalent cations *Biomacromolecules* **11** 2966–75
[61] Sikorski P, Mo F, Skjåk-Braek G and Stokke B T 2007 Evidence for egg-box-compatible interactions in calcium-alginate gels from fiber x-ray diffraction *Biomacromolecules* **8** 2098–103
[62] Jarand A R, Jarand C W and Reed W F 2026 Miniature conductivity and pH sensors using ion selective field effect transistors applied in cuvette-based dialysis spectroscopy *Meas. Sci. Technol.* **37** 045104